

# Synthesis of Fluoride-Containing High Dimensionally Structured Nb Oxide and Its Catalytic Performance for Acid Reactions

Satoshi Ishikawa,\* Mai Shinoda, Yuta Motoki, Shota Tsurumi, Momoka Kimura, Norihito Hiyoshi, Akihiro Yoshida, and Wataru Ueda\*

Cite This: <https://dx.doi.org/10.1021/acs.inorgchem.0c00949>

Read Online

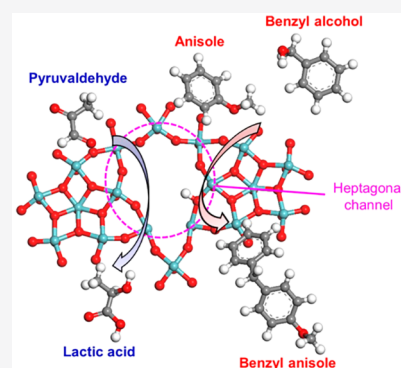
ACCESS |

Metrics & More

Article Recommendations

Supporting Information

**ABSTRACT:** High dimensionally structured niobium oxide (HDS-NbO) containing fluoride ( $F^-$ ) was prepared by a hydrothermal synthesis.  $F^-$  could be introduced into HDS-NbO by replacing lattice oxygen up to a solid  $F^-/Nb$  ratio of 0.55. The introduction of an appropriate amount of  $F^-$  promoted the crystal growth of HDS-NbO, while niobium oxyfluoride having the hexagonal tungsten bronze structure (HTB-Nb( $F,O$ ))<sub>x</sub> was concomitantly formed by excess  $F^-$  addition. HAADF-STEM analysis suggested that the number of micropores (hexagonal and heptagonal channels) in HDS-NbO was increased by the introduction of an appropriate amount of  $F^-$ . The catalytic activity for Brønsted acid reactions was evaluated by Friedel–Crafts alkylation. The catalytic activity was significantly increased by the introduction of  $F^-$ , while excess introduction of  $F^-$  significantly decreased the activity. Catalytic activity for the Lewis acid reaction in the presence of water was evaluated by the transformation of pyruvaldehyde into lactic acid. The catalytic activity was changed by the introduction of  $F^-$  in a manner similar to that observed in the Friedel–Crafts alkylation. On the basis of the results obtained, we propose that the local catalyst structure around the micropores of HDS-NbO is crucial for the acid reactions.



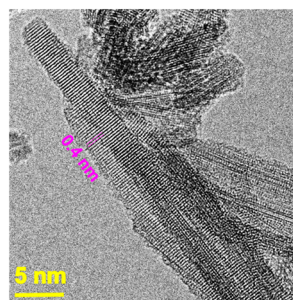
## 1. INTRODUCTION

Niobium oxide (NbO) is well-known as a unique acid catalyst showing significantly strong Brønsted acidity comparable to 70% sulfuric acid solution.<sup>1–3</sup> Many efforts have been made to identify the origin of its unique acid property.<sup>3–8</sup> However, the catalytic properties over NbO are still a matter of debate despite tremendous efforts. There are two main reasons for the difficulty in clarifying its acid properties. The first reason is the amorphous nature of NbO. The amorphous nature of NbO makes it difficult to investigate the catalytically active sites, since only limited information can be obtained due to the inherent heterogeneity of the catalytically active sites. The second reason is methods for characterization of the acid properties. Although many methods for characterization have been proposed so far, it is still difficult to clearly evaluate the nature of true active sites for catalytic reactions since conventional characterization methods sometimes detect acid sites that are inactive for catalysis. These problems have been masking the true catalytically active sites over NbO.

We recently reported the synthesis and characterizations of high dimensionally structured niobium oxide (HDS-NbO).<sup>9,10</sup> This material is constituted by structural arrangements based on  $\{Nb_6O_{21}\}^{12-}$  pentagonal units and  $\{NbO_6\}$  octahedra to form a rod-shaped crystal by stacking of the above units along the rod direction with an interval distance of ca. 0.4 nm. Due to its structural arrangement, micropores (hexagonal and heptagonal channels) are formed in the cross section of the rod

(Figure 1). HDS-NbO showed outstanding catalytic activity for Brønsted acid reactions, as evaluated by Friedel–Crafts

(A)



(B)

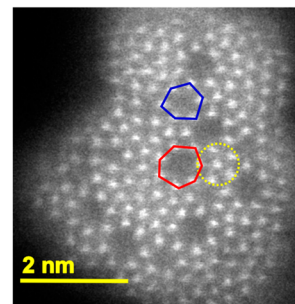


**Figure 1.** HAADF-STEM images of HDS-NbO in a side section (A) and a cross section (B) of the rod. The  $\{Nb_6O_{21}\}^{12-}$  pentagonal unit is marked as a yellow dotted circle. A hexagonal channel and a heptagonal channel are represented as blue and red enclosures, respectively.

Received: April 1, 2020

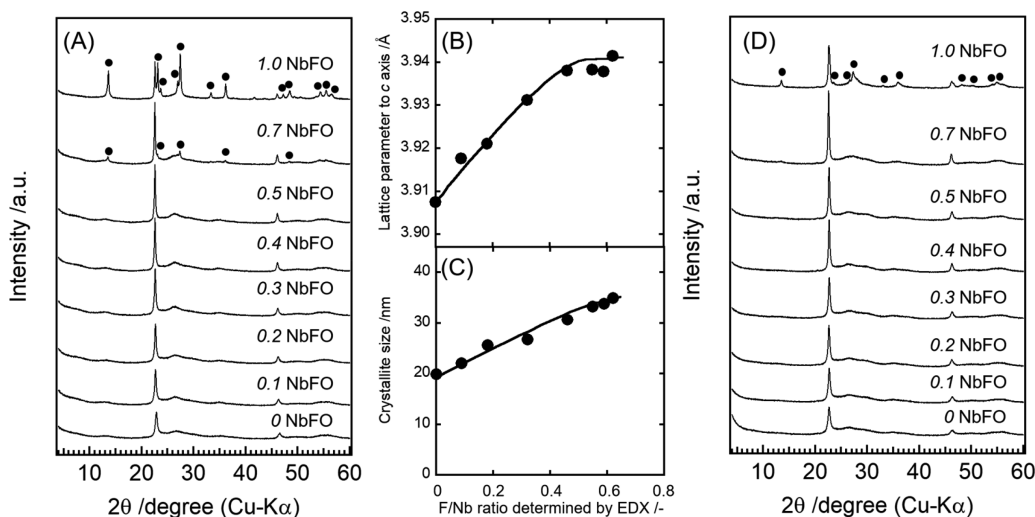


**Figure 2.** (A) XRD patterns of as-synthesized  $x\text{NbFO}$ . Changes in the lattice parameter to the  $c$  axis (B) and crystallite size (C) as a function of F/Nb ratio in as-synthesized  $x\text{NbFO}$  determined by the XRD peak derived from the (001) plane of HDS-NbO. (D) XRD patterns of  $x\text{NbFO}$  after air calcination at 400 °C for 2 h. Solid circles in (A) and (D) indicate the XRD peaks of HTB-Nb(F,O) $_x$ .

alkylations, and for Lewis acid reactions in the presence of water, as evaluated by the transformation of pyruvaldehyde to lactic acid.<sup>9,10</sup> Since the activity was much higher than that of other Nb oxide catalysts even on a surface area basis, the local crystal structure over HDS-NbO was suggested to be responsible for its catalysis.<sup>9</sup> However, the true catalytically active sites over HDS-NbO were still unclear, since the contributions of various structural sites (e.g., the pentagonal  $\{\text{Nb}_6\text{O}_{21}\}^{12-}$  unit,  $\{\text{NbO}_6\}$  octahedra, and micropores) to its catalysis have not been elucidated.

Here, we synthesized HDS-NbO containing  $\text{F}^-$  inside the crystal structure (HDS-NbFO). The introduction of an appropriate amount of  $\text{F}^-$  increased the number of micropore sites in the HDS-NbO structure, while excess addition of  $\text{F}^-$  caused concomitant formation of a niobium oxyfluoride having the hexagonal tungsten bronze structure (HTB-Nb(F,O) $_x$ ). The catalytic activity for Brønsted acid reactions (Friedel–Crafts alkylation) and Lewis acid reactions in the presence of water (pyruvaldehyde transformation) was significantly increased on the basis of the surface area by the introduction of an appropriate amount of  $\text{F}^-$ , while the activity was decreased by excess addition of  $\text{F}^-$ . On the basis of the results obtained, we propose that a specific structural part in HDS-NbO is crucial for the above reactions and that the acid sites formed around the micropore sites are responsible for the catalysis of these reactions.

## 2. EXPERIMENTAL SECTION

**2.1. Synthesis of High Dimensionally Structured Niobium Oxide Containing Fluoride.** High dimensionally structured niobium oxide containing fluoride (HDS-NbFO) was prepared by a conventional hydrothermal method using an aqueous ammonium niobium oxalate (ANO,  $\text{NH}_4(\text{NbO}(\text{C}_2\text{O}_4)_2(\text{H}_2\text{O})_2 \cdot n\text{H}_2\text{O}$ ; Sigma-Aldrich) solution.<sup>9,10</sup> First, 6 mmol of ANO was dissolved in 40 mL of deionized water. To the ANO solution was added  $a$  mmol ( $a = 0$ –6) of  $\text{NH}_4\text{F}$  (Wako), and the solution was stirred for 10 min at room temperature. The resulting solution was transferred to a Teflon inner tube (50 mL), and then hydrothermal synthesis was conducted at 175 °C for 72 h. The obtained white precipitate was washed with 500 mL of deionized water and then dried at 80 °C overnight. The materials obtained are abbreviated as  $x\text{NbFO}$ , where  $x$  represents the

preparative F/Nb ratio. Prior to the catalytic reactions,  $x\text{NbFO}$  was calcined at 400 °C for 2 h under static air.

**2.2. Characterization of Materials.** The materials obtained were characterized by the following techniques. Powder XRD patterns were recorded with a diffractometer (RINT Ultima+, Rigaku) using Cu  $K\alpha$  radiation (tube voltage, 40 kV; tube current, 20 mA). Diffractions were recorded in the range of 4–60° with a 5°  $\text{min}^{-1}$  scan speed. SEM-EDX analysis was carried out with an electron microscope (SU8010, Hitachi) equipped with an EDX detector (EMAX Evolution X-MAX, Horiba). XPS (JPC-9010MC, JEOL) with nonmonochromatic Mg  $K\alpha$  radiation was used for measuring the elemental composition over the catalyst surface.  $\text{N}_2$  adsorption isotherms at liquid  $\text{N}_2$  temperature were obtained using an autoadsorption system (BELSORP MAX, BEL JAPAN). Prior to the  $\text{N}_2$  adsorption, the samples were pretreated under vacuum conditions at 400 °C for 2 h. The surface area was determined by a multipoint Brunauer–Emmett–Teller (BET) method using the adsorption range of  $0.05 \leq P/P_0 \leq 0.30$ . Aberration-corrected STEM images were obtained using ARM-200F (JEOL Ltd., Japan) equipped with a cold field emission gun at an acceleration voltage of 200 kV. Temperature-programmed desorption (TPD) was carried out by using an autochemisorption system (BEL JAPAN). The sample (ca. 50 mg) was sandwiched by two layers of quartz wool. The temperature was increased from 40 to 600 °C with 50  $\text{mL min}^{-1}$  of He flow. Pyridine adsorption FT-IR analysis was carried out using a gas flow system equipped with a spectrometer (FT/IR-6100, JASCO). For analysis, a sample disk (ca. 40 mg, disk diameter 20 mm) was set at the IR cell, and the temperature was increased with a ramp of 10 °C/min to 400 °C under 50  $\text{mL min}^{-1}$  of He flow. After the temperature was kept at 400 °C for 10 min, the temperature was decreased to 100 °C under the same gas flow condition. Then 0.2  $\mu\text{L}$  of pyridine was injected from the top of the IR cell and the injection was repeated until the IR band intensity became constant. IR spectra were obtained on an MCT detector by integration of 128 scans with a resolution of 4  $\text{cm}^{-1}$ . After the pyridine adsorption IR experiment, 10 mg of the sample was subjected to TG measurement (Thermo plus EVO2, Rigaku) under 100  $\text{mL min}^{-1}$  of air flow. The amount of adsorbed pyridine was estimated on the basis of the weight loss from ca. 150 °C to ca. 500 °C. The amounts of Brønsted acid sites and Lewis acid sites were separately calculated by taking into account (1) the area of IR bands assignable to the pyridine adsorbed on Brønsted acid sites (1540  $\text{cm}^{-1}$ ) or on Lewis acid sites (1445  $\text{cm}^{-1}$ ), (2) the molar extinction coefficients for infrared adsorption bands,<sup>11,12</sup> and (3) the amount of adsorbed pyridine measured by the TG experiment. The acid strength was evaluated using the Hammett

Table 1. Physicochemical Properties of  $x$ NbFO

catalyst	crystallite size <sup>a</sup> /nm	BET surface area <sup>b</sup> /m <sup>2</sup> g <sup>-1</sup>	F/Nb ratio <sup>c</sup>		amt of NH <sub>3</sub> desorbed <sup>d</sup> /mmol g <sup>-1</sup>
			EDX	XPS	
0NbFO	19.9 (18.5)	233			880
0.1NbFO	22.0 (20.9)	206	0.09 (0.02)	0.11 (0.06)	968
0.2NbFO	25.6 (22.3)	187	0.18 (0.06)	0.15 (0.08)	1058
0.3NbFO	26.8 (23.4)	176	0.32 (0.09)	0.18 (0.10)	997
0.4NbFO	30.6 (25.6)	175	0.46 (0.12)	0.24 (0.04)	1113
0.5NbFO	33.2 (27.6)	150	0.55 (0.10)	0.17 (0.12)	1038
0.7NbFO	34.9 (31.5)	131	0.62 (0.29)	0.43 (0.37)	1343
1.0NbFO	33.8 (24.0)	59	0.59 (0.47)	1.78 (0.72)	2003

<sup>a</sup>Crystallite size of HDS-NbO determined by using the XRD peak at  $2\theta = 22.7^\circ$  before air calcination is shown. Crystallite size after the calcination is shown in parentheses. <sup>b</sup>Measured by N<sub>2</sub> adsorption at liquid N<sub>2</sub> temperature and determined by the BET method. <sup>c</sup>F/Nb ratios before air calcination are shown and F/Nb ratios after air calcination at 400 °C are shown in parentheses. <sup>d</sup>Measured by TPD.

indicator. Catalysts were immersed in a liquid solution containing 4-(phenylazo)diphenylamine ( $pK_a = 1.5$ ), dicinnamal acetone ( $pK_a = -3.0$ ), chalcone ( $pK_a = -5.6$ ), and anthraquinone ( $pK_a = -8.1$ ), and the solution color was checked.<sup>13</sup>

**2.3. Catalytic Reaction.** **2.3.1. Friedel–Crafts Alkylation.** First, a mixture of benzyl alcohol (1 mmol, TCI), anisole (45 mmol, Wako), and decane (an internal standard, 0.5 mmol, Wako) was placed in a 20 mL flask. Then 20–50 mg of the catalyst and a Teflon-coated magnetic stir bar were loaded into a reactor. The flask was set with the reactor preheated at 100 °C, and stirring with the magnetic stir bar was performed at a rate of 600 rpm. The reaction time was measured from the time when the flask was placed in the reactor. Aliquots (0.2 mL each) were collected at intervals. The amounts of the reactant and the product were measured by gas chromatography using a flame ionization detector (GC-2010, Shimadzu) with a TC-WAX column (0.25 mm  $\times$  30 m).

**2.3.2. Transformation of Pyruvaldehyde to Lactic Acid.** First, a mixture of pyruvaldehyde (0.5 mmol, Sigma-Aldrich) and distilled water (5 mL) was placed in a 20 mL flask. Then 25 mg of the catalyst and a Teflon-coated magnetic stir bar were loaded into the reactor. The flask was set with the reactor preheated at 100 °C, and stirring with the magnetic stir bar was performed at a rate of 600 rpm. The reaction time was measured from the time when the flask was placed in the reactor. Aliquots (0.2 mL each) were collected at intervals. The amounts of the reactant and the product were measured by high-performance liquid chromatography with a refractive index detector (RID-20A, Shimadzu) and with a HPX-87H column (300 mm  $\times$  7.8 mm) by using citric acid as the external standard.

### 3. RESULTS AND DISCUSSION

**3.1. Synthesis and Characterizations of  $x$ NbFO.** XRD patterns of as-synthesized  $x$ NbFO are shown in Figure 2A. 0NbFO shows characteristic XRD peaks at  $2\theta = 22.8$  and  $46.8^\circ$ . These peaks are commonly observed in the materials formed on the basis of the stacking of octahedra (e.g., crystalline Mo<sub>3</sub>VO <sub>$x$</sub> , high dimensionally structured MoFeO), indicating that HDS-NbO is comprised of the stacking of octahedra with an interval distance of ca. 0.39 nm.<sup>9,10,14,15</sup> At  $0.1 \leq x \leq 0.5$ , XRD peak intensities at  $2\theta = 22.8$  and  $46.8^\circ$  were increased and downward shifts in these peaks were observed. Since the XRD pattern of HDS-NbO was almost the same despite the addition of NH<sub>4</sub><sup>+</sup> by using (NH<sub>4</sub>)<sub>2</sub>SO<sub>4</sub> (preparative (NH<sub>4</sub>)<sub>2</sub>SO<sub>4</sub>/Nb molar ratio 0.25), F<sup>-</sup> was found to increase the crystallinity of HDS-NbO (Figure S1). SEM-EDX measurements were carried out for 0NbFO, 0.5NbFO, and 1.0NbFO (Figure S2). These materials were rod-shaped crystals derived from the stacking of {NbO<sub>6</sub>} octahedra, as we reported previously.<sup>9,10</sup> The diameter of the rods was increased by the introduction of F<sup>-</sup> from ca. 6 nm in 0NbFO to ca. 15

nm in 0.5NbFO as estimated by SEM images. In the case of 1.0NbFO, rod-shaped crystals formed from the hexagonal-shaped particles were observed (Figure S2D) as well as crystals having a crystal morphology similar to that of 0.5NbFO (Figure S2C). Elemental compositions of  $x$ NbFO were measured by EDX (bulk) and XPS (surface). In the case of EDX, the elemental composition of the rod-shaped crystals derived from HDS-NbFO was measured. The measured elemental compositions are shown in Table 1. In both cases, the F/Nb ratio increased with an increase in  $x$ . Figure 2B shows the relationship between the lattice parameter to the  $c$  axis and the F/Nb ratio in the solid. The lattice parameter to the  $c$  axis increased proportionally with an increase in the F/Nb ratio in the solid up to an F/Nb ratio of 0.55. The increase in the lattice parameter implies the replacement of constituent elements with another element having a different ion radius. In the present case, O<sup>2-</sup> in {NbO<sub>6</sub>} octahedra is thought to be replaced with F<sup>-</sup> up to an F/Nb ratio of 0.55. In addition to the increase in the lattice parameter, the crystallite size of HDS-NbFO estimated by the Scherrer equation ( $2\theta = 22.8^\circ$ ) increased linearly with an increase in the F/Nb ratio in the solid (Figure 2C). The results of an N<sub>2</sub> adsorption experiment supported this observation, since the BET surface area of  $x$ NbFO decreased in the order of the crystallite size (Table 1). The addition of NH<sub>4</sub>F above  $0.7 \leq x$  had a slight effect on the crystallite size and lattice parameter of the HDS-NbO structure, and new XRD peaks appeared at  $2\theta = 13.6, 23.2, 23.7, 26.9, 27.4, 33.4,$  and  $36.1^\circ$ . These peaks are attributed to the conventional hexagonal tungsten bronze (HTB) structure.<sup>16,17</sup> Therefore, the materials showing the above XRD peaks are hereafter denoted as HTB-Nb(F,O) <sub>$x$</sub> . Further addition of NH<sub>4</sub>F increased the XRD peak intensities of HTB-Nb(F,O) <sub>$x$</sub>  without changing the crystallite size and lattice parameter of the HDS-NbO structure. We concluded that the introduction of F<sup>-</sup> significantly influenced the crystal formation of HDS-NbO.

Then  $x$ NbFO was calcined at 400 °C for 2 h under an air atmosphere. The amount of F<sup>-</sup> was significantly decreased after air calcination (Table 1), and the F/Nb ratio measured by EDX was  $0 \leq \text{F/Nb} \leq 0.12$  at  $0 \leq x \leq 0.5$ . Although desorption species related to F<sup>-</sup> were difficult to identify, HF is the possible desorbed species. The F/Nb ratio at  $0.7 \leq x$  was considerably higher than those at  $0 \leq x \leq 0.5$  after air calcination, and the ratios were 0.29 and 0.47 for 0.7NbFO and 1.0NbFO, respectively. F<sup>-</sup> species might be stably accommodated at the hexagonal moiety in HTB-Nb(F,O) <sub>$x$</sub>  that was concomitantly formed with HDS-NbFO, and such F<sup>-</sup> is

thought to be hardly removed by calcination. The F/Nb ratio evaluated by XPS analysis was also decreased by calcination in a manner similar to that measured by EDX, indicating that significant amounts of  $F^-$  species were removed from the catalyst surface by air calcination. XRD patterns of  $x\text{NbFO}$  after air calcination at  $400\text{ }^\circ\text{C}$  for 2 h are shown in Figure 2D. XRD patterns were almost unchanged after air calcination at  $0 \leq x \leq 0.5$ . In fact, the crystallite size of  $x\text{NbFO}$  was almost the same regardless of air calcination (Table 1). However, the lattice parameter to the  $c$  axis was changed after the calcination and the lattice parameters became comparable regardless of the value of  $x$  (Figure S3). The removal of  $F^-$  from the crystal structure should be related to its lattice parameter change. The XRD pattern at  $0.7 \leq x$  was very different after air calcination, and the XRD peak intensities related to  $\text{HTB-Nb}(\text{F},\text{O})_x$  were significantly decreased, possibly due to the amorphization as shown later, while the XRD peaks derived from HDS-NbFO were almost unchanged.

TEM and HAADF-STEM analyses were then conducted for  $0.5\text{NbFO}$  and  $1.0\text{NbFO}$  in order to investigate the local crystal structure. These analyses were conducted for samples after air calcination at  $400\text{ }^\circ\text{C}$  for 2 h. Figure 3A shows a TEM image of

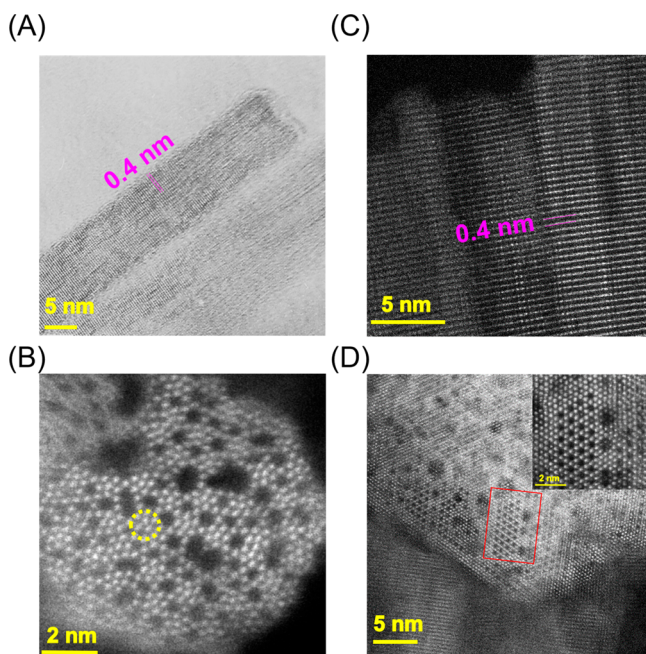


**Figure 3.** TEM (A) and HAADF-STEM images (B–D) of  $0.5\text{NbFO}$  (A, B) and  $1.0\text{NbFO}$  (C, D). The insert in (D) is a magnified image of the red square. The  $\{\text{Nb}_6\text{O}_{21}\}^{12-}$  pentagonal unit is marked by a yellow dotted circle in (B).

$0.5\text{NbFO}$ . This material was a rod-shaped crystal showing a lattice fringe for the rod direction with an internal distance of ca.  $0.4\text{ nm}$ , being consistent with the XRD results. The observed lattice fringe indicates periodic stacking of  $\{\text{NbO}_6\}$  octahedra with a corner-sharing manner along the rod direction. The diameter of the rod estimated from this image was ca.  $11\text{ nm}$ , which was clearly larger than that of  $0\text{NbFO}$  (ca.  $3\text{ nm}$ , Figure 1), implying an increase in the diameter by the introduction of  $F^-$ , as was also seen in the SEM images. Then the local crystal structure in a cross section was measured from the (001) direction, and the obtained HAADF-STEM image of  $0.5\text{NbFO}$  is shown in Figure 3B. Since the contrast

observed in the HAADF-STEM image is roughly proportional to the atomic number of the elements, the white spots in the image indicate the location of Nb and the dark spots indicate the pores produced by the arrangement of  $\{\text{NbO}_6\}$  octahedra. The diameter of the cross section of  $0.5\text{NbFO}$  was ca.  $11\text{ nm}$ , which is quite consistent with the average diameter of the rods estimated by the SEM images. Therefore, we believe that the crystal we measured is the representative crystal as  $0.5\text{NbFO}$ . The cross section of  $0.5\text{NbFO}$  was constituted by the arrangement of  $\{\text{Nb}_6\text{O}_{21}\}^{12-}$  pentagonal units and  $\{\text{NbO}_6\}$  octahedra, forming micropores such as hexagonal and heptagonal pores in the structure. In the case of  $0.5\text{NbFO}$ , the  $\{\text{Nb}_6\text{O}_{21}\}^{12-}$  pentagonal units were isolated from each other by  $\{\text{NbO}_6\}$  octahedral linkers, and the number of micropores in the crystal structure seems to be increased in comparison with that in  $0\text{NbFO}$  (structural images of  $0\text{NbFO}$  and  $0.5\text{NbFO}$ : Figure 4). In fact, the numbers of hexagonal

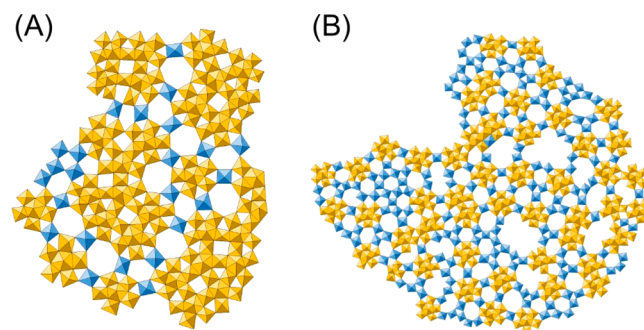


**Figure 4.** Structural images of  $0\text{NbFO}$  (A) and  $0.5\text{NbFO}$  (B) created by using their HAADF-STEM images (Figures 1 and 3B). Color scheme: yellow,  $\{\text{Nb}_6\text{O}_{21}\}^{12-}$  pentagonal units; blue,  $\{\text{NbO}_6\}$  octahedra.  $\{\text{Nb}_6\text{O}_{21}\}^{12-}$  pentagonal units were well isolated in  $0.5\text{NbFO}$  due to the change in the coordination state around Nb atoms by replacing  $\text{O}^{2-}$  with  $\text{F}^-$ .

and heptagonal channels estimated by HAADF-STEM images were  $0.26/\text{nm}^2$  and  $0.18/\text{nm}^2$  for  $0\text{NbFO}$  and  $0.50/\text{nm}^2$  and  $0.50/\text{nm}^2$  for  $0.5\text{NbFO}$ , respectively. TPD measurement was then carried out in order to support these experimental observations (Table 1). In the TPD experiment, an  $\text{NH}_3$  desorption profile centered at ca.  $320\text{ }^\circ\text{C}$  was observed in all of the  $x\text{NbFO}$  samples (Figure S4). The amount of desorbed  $\text{NH}_3$  estimated from the  $\text{NH}_3$  desorption peak area was  $880\text{ }\mu\text{mol g}^{-1}$  in  $0\text{NbFO}$ . This amount was increased by the introduction of  $F^-$ , and the amount was  $968\text{--}1113\text{ }\mu\text{mol g}^{-1}$  at  $0.1 \leq x \leq 0.5$ . Theoretically, this amount should be decreased by an increase in  $x$ , since a decrease in the solid anionic charge caused by the replacement of  $\text{O}^{2-}$  with  $\text{F}^-$  should decrease the number of counteranions ( $\text{NH}_4^+$ ). Therefore, the observed increase in the amount of  $\text{NH}_3$  desorption suggests an increase in the structural sites where  $\text{NH}_4^+$  can be accommodated. We have reported that  $\text{NH}_3$  desorption takes place around  $300\text{ }^\circ\text{C}$  from the heptagonal channel of crystalline  $\text{Mo}_3\text{VO}_x$  material ( $\text{MoVO}$ ) that is constituted by pentagonal units and octahedra in a manner similar to that for HDS-NbO.<sup>18–20</sup> On the basis of the structural similarity between HDS-NbO and  $\text{MoVO}$ , the observed TPD profile should be derived from the  $\text{NH}_3$  desorption from micropores of HDS-NbFO. Accordingly, the increase in the amount of  $\text{NH}_3$  desorption by the introduction of  $F^-$  should indicate an increase in the number of micropores in the solid. On the basis of these results, we concluded that

the number of micropores in HDS-NbFO was increased by the introduction of an appropriate amount of  $F^-$ . The increase in the number of micropores might be caused by local structural changes derived from the changes in the sharing state of  $\{NbO_6\}$  octahedra. The replacement of  $O^{2-}$  with  $F^-$  is expected to increase the coordination number of Nb atoms due to the decreased anionic charge, which should promote the changes in the sharing state of the octahedra from an edge or face sharing to corner sharing.<sup>21–23</sup> This local coordination state change would contribute to the isolation of pentagonal  $\{Nb_6O_{21}\}^{12-}$  units to promote the formation of micropores, as can be seen in the HAADF-STEM images. The increase in crystallite size is also explainable, since corner sharing is normally energetically more stable than are edge sharing and face sharing, which cause an unfavorable repulsion between cations due to the small distance.

HAADF-STEM images of 1.0NbFO are shown in Figure 3C,D. This material was also a rod-shaped material showing a lattice fringe for the rod direction with an internal distance of ca. 0.4 nm, indicative of the stacking of octahedra (Figure 3C). Figure 3D shows a cross section of the rod-shaped crystal having a hexagonal-shaped morphology. In the hexagonal-shaped crystal, an HTB-Nb(F,O)<sub>x</sub> texture was partially observed, as can be seen in the magnified image in Figure 3D, while a large part of the crystal was disordered. The observed disordered structure might be caused by an amorphization of the HTB-Nb(F,O)<sub>x</sub> structure by the air calcination conducted prior to the HAADF-STEM measurement, as could be seen in XRD analysis.

On the basis of the results described above, it was found that the introduction of an appropriate amount of  $F^-$  into HDS-NbO enhanced the crystal growth and increased the number of micropores in the crystal structure. However, the introduction of an excess amount of  $F^-$  induced the formation of HTB-Nb(F,O)<sub>x</sub>. In the next section, acid properties over  $x$ NbFO will be discussed.

**3.2. Acid Properties over  $x$ NbFO.** Here, acid properties over the catalyst surface of  $x$ NbFO are evaluated. Prior to characterizations,  $x$ NbFO samples were calcined at 400 °C under static air. Almost all of the  $NH_4^+$  was removed from the structure of  $x$ NbFO, since almost no IR band derived from  $NH_4^+$  deformation (1401  $cm^{-1}$ ) was observed in HDS-NbO with  $0.1 \leq x \leq 0.5$  after air calcination (Figure S5), while a small band derived from  $NH_4^+$  was observed at  $0.7 \leq x$ . Nevertheless, Brønsted acid sites (B sites) are expected to be formed over  $x$ NbFO.

$NH_3$  adsorption TPD measurements are often conducted for the characterization of acid properties.<sup>24–26</sup> This is quite a useful method to evaluate the acid properties over a catalyst. However, this method is considered not to be appropriate for  $x$ NbFO, since this material has micropores that are capable of adsorbing  $NH_3$  and the amount of acid from the bulk would be evaluated as well as that from the catalyst surface. Therefore, we needed to use the base prove molecule inaccessible inside the micropores in order to evaluate the acid properties over the surface of  $x$ NbFO. For this purpose, a pyridine adsorption IR experiment was carried out. This method is useful for distinguishing the type of acid site (either Brønsted acid site (B site) or Lewis acid site (L site)), since pyridine adsorbed over the B site and that adsorbed over the L site give different IR bands.<sup>27,28</sup> The IR spectra of 0NbFO and 0.5NbFO after pyridine adsorption are shown in Figure 5A. Both of the catalysts showed IR bands at 1540  $cm^{-1}$  assignable to

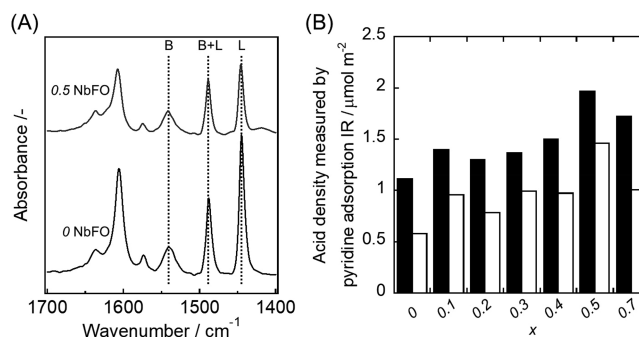


**Figure 5.** (A) IR spectra of 0NbFO and 0.5NbFO after pyridine adsorption. (B) Amount of acid at the Lewis site (L site, black bars) and Brønsted acid site (B site, white bars) over  $x$ NbFO calculated on the basis of surface area.

pyridinium ions formed on the B site and at 1445  $cm^{-1}$  assignable to coordinated pyridine on the L site. The amounts of B and L sites were calculated on the basis of the weight loss derived from pyridine (Figure S6) and the molar extinction coefficients for IR bands of the B site and L site ( $\epsilon_B/\epsilon_L = 1.33$ ), respectively.<sup>11,12</sup> The acid amounts of 0NbFO estimated according to this method were comparable to the reported values (reported values, B site  $0.09 \pm 0.01$  mmol  $g^{-1}$ , L site  $0.20 \pm 0.01$  mmol  $g^{-1}$ ; estimated values, B site 0.13 mmol  $g^{-1}$ , L site 0.25 mmol  $g^{-1}$ ).<sup>10</sup> The environment around the Lewis acid in  $x$ NbFO should be similar, as can be seen in almost the same shape of the absorption band at 1610  $cm^{-1}$ , which is sensitively changed in a reflection of the environment around the Lewis acid site.<sup>29,30</sup> Figure 5B shows the amounts of B and L sites on the basis of the surface area. The amounts of both B and L sites were increased by an increase of  $x$  up to 0.5, while the amounts of both sites were slightly decreased at  $x = 0.7$ . A local structural change over the catalyst surface might be related to the observed changes. The amount of acid over 1.0NbFO was difficult to estimate, since it was quite difficult to make an IR disk of 1.0NbFO itself unless a binder (KBr) was mixed. The band area ratios of 1540 and 1445  $cm^{-1}$ ,  $A_{1540}/A_{1445}$ , over  $x$ NbFO are shown in Figure S7. The  $A_{1540}/A_{1445}$  ratios were comparable at  $0 \leq x \leq 0.7$ , indicating that the ratios of the B site and L site over the catalyst surface are comparable. However, the  $A_{1540}/A_{1445}$  ratio over 1.0NbFO was slightly smaller than those at  $0 \leq x \leq 0.7$ . The coformation of HTB-Nb(F,O)<sub>x</sub> moieties in 1.0NbFO might be related to this change.

The acid strength over  $x$ NbFO was evaluated by the Hammett indicator. The results obtained are summarized in Table S1.  $x$ NbFO showed comparable acid strengths at  $0 \leq x \leq 0.7$ , and they were in the range of  $-8.2 < pK_a \leq -5.6$ . However, the acid strength over 1.0NbFO was smaller than those of other  $x$ NbFO samples, and the strengths were  $-5.6 < pK_a \leq -3.0$ . The amorphized HTB-Nb(F,O)<sub>x</sub> texture might form weaker acid sites in comparison to those formed over HDS-NbO. On the basis of the above results, we concluded that the amount of acid over the catalyst surface of HDS-NbFO was increased by the introduction of an appropriate amount of  $F^-$ , while the acid strength was not changed drastically other than for 1.0NbFO. In the next section, the catalytic activities over  $x$ NbFO for Brønsted acid reactions and Lewis acid reactions will be discussed.

**3.3. Acid Reactions over  $x$ NbFO.** As described above, it was found that the addition of an appropriate amount of  $F^-$

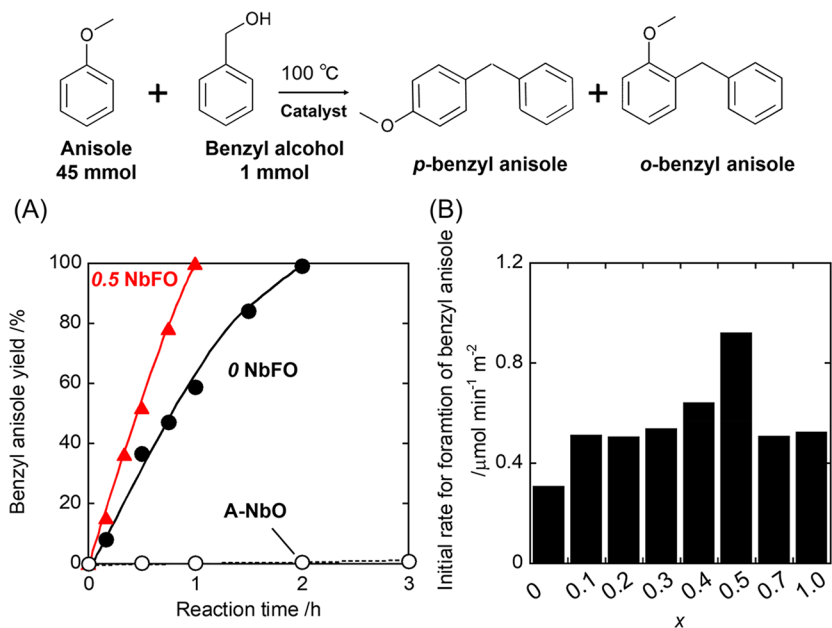


**Figure 6.** (A) Benzyl anisole yields on the basis of benzyl alcohol as a function of reaction time over A-NbO, 0NbFO, and 0.5NbFO. Reaction conditions: benzyl alcohol/anisole/decane (internal standard), 1.0/45/0.5 mmol; catalyst amount, 0.050 g; reaction temperature, 100 °C. (B) Initial formation rate of benzyl anisole over  $x\text{NbFO}$ . Reaction conditions: benzyl alcohol/anisole/decane (internal standard), 1.0/45/0.5 mmol; catalyst amount, 0.020–0.033 g; reaction temperature, 100 °C; reaction time, 0–30 min.

modified the local crystal structure of HDS-NbO and increased the number of micropore sites in the crystal structure. The acid properties evaluated by pyridine adsorption IR and Hammett indicator experiments revealed that the acid amount was changed by the introduction of  $\text{F}^-$ , while the strengths were comparable at  $0 \leq x \leq 0.7$ . Catalytic activities for Brønsted acid reactions (B reactions) and Lewis acid reactions (L reactions) were evaluated over  $x\text{NbFO}$ .

As a B reaction, Friedel–Crafts alkylation was carried out by using anisole and benzyl alcohol as substrates. This reaction is widely used as a model reaction to elucidate the catalytic activity for a B reaction, since a B site can promote the formation of an alkylation product (benzyl anisole).<sup>9,31,32</sup>  $x\text{NbFO}$  samples after calcination at 400 °C for 2 h under an air atmosphere were used as catalysts for this reaction. Amorphous  $\text{Nb}_2\text{O}_5 \cdot 2.1\text{H}_2\text{O}$  (A-NbO) calcined at 250 °C for 2 h under an air atmosphere was used for comparison with  $x\text{NbFO}$ , since it is well-known to be an effective catalyst for various acid reactions.<sup>33</sup> The acid amount and acid strength over A-NbO after the calcination were also evaluated by pyridine adsorption IR and Hammett indicator. Figure S8A shows the results of pyridine adsorption IR over A-NbO. IR bands derived from the adsorption of pyridine on the B site ( $1540 \text{ cm}^{-1}$ ) and on the L site ( $1445 \text{ cm}^{-1}$ ) were observed, and the amounts of B and L sites were calculated by TG analysis (Figure S8B); and the molar extinction coefficients for IR bands of B and L sites were 1.0 and  $0.4 \mu\text{mol}/\text{m}^2$ , respectively (BET surface area:  $130 \text{ m}^2/\text{g}$ ). The ratio of the areas of IR bands derived from pyridine adsorption over B and L sites ( $A_{1540}/A_{1445}$ ) was 2.6, comparable with that of  $x\text{NbFO}$  ( $0 \leq x \leq 0.7$ ). The acid strength estimated by the Hammett indicator was  $-8.2 < \text{p}K_{\text{a}} \leq -5.6$  and was similar to that of  $x\text{NbFO}$ .

In the Friedel–Crafts alkylation, all of the catalysts tested afforded benzyl anisole as a main product and only a tiny amount of benzyl ether was formed (less than 3% selectivity in all cases), indicating that the B site over  $x\text{NbFO}$  dominantly

catalyzed the reaction.<sup>31,32</sup> Figure 6A shows the benzyl anisole yields on the basis of benzyl alcohol as a function of reaction time over 0NbFO, 0.5NbFO, and A-NbO. A-NbO was almost inactive for this reaction, and almost no benzyl anisole was formed. However, benzyl anisole was formed over 0NbFO and the benzyl anisole yield increased with an increase in reaction time. The reaction was almost complete at 2 h from the start of the reaction. Interestingly, the benzyl anisole yield over 0.5NbFO was much higher than that over 0NbFO and the reaction was almost complete within 1.0 h. Although the acid properties, including the acid densities and acid strengths, were similar over 0NbFO, 0.5NbFO, and A-NbO, the catalytic activities were very different. The initial formation rate of benzyl anisole was then measured over  $x\text{NbFO}$ . Note that the reaction rate was obtained in the range in which the yield of benzyl anisole increased linearly with reaction time (Figure S9; benzyl anisole yield below 15%). Figure 6B shows the initial formation rate of benzyl anisole over  $x\text{NbFO}$  on the basis of the surface area. In the case of 0NbFO, the initial formation rate on the basis of the surface area was  $0.31 \mu\text{mol min}^{-1} \text{m}^{-2}$ . This rate continuously increased with an increase in  $x$ , and a rate of  $0.92 \mu\text{mol min}^{-1} \text{m}^{-2}$  was achieved over 0.5NbFO, 3 times higher than that over 0NbFO. On the other hand, the rate was significantly decreased by a further increase in  $x$  and the rate was  $0.52 \mu\text{mol min}^{-1} \text{m}^{-2}$  over 1.0NbFO. The catalytic activity changed with  $x$  in a manner similar to the amount of acid estimated by pyridine adsorption IR. We reported that HDS-NbO showed clearly higher catalytic activity for Friedel–Crafts alkylation in comparison to the catalytic activities of other Nb-based oxides such as T-Nb<sub>2</sub>O<sub>5</sub> and pyrochlore.<sup>9</sup> On the basis of these results, we suggested that the local catalyst structure over HDS-NbO is responsible for the catalysis. In the present study, local structural changes caused by the introduction of  $\text{F}^-$  were suggested by the results of HAADF-STEM analysis, and it was found that the number of micropores was increased by the introduction of  $\text{F}^-$ . On the

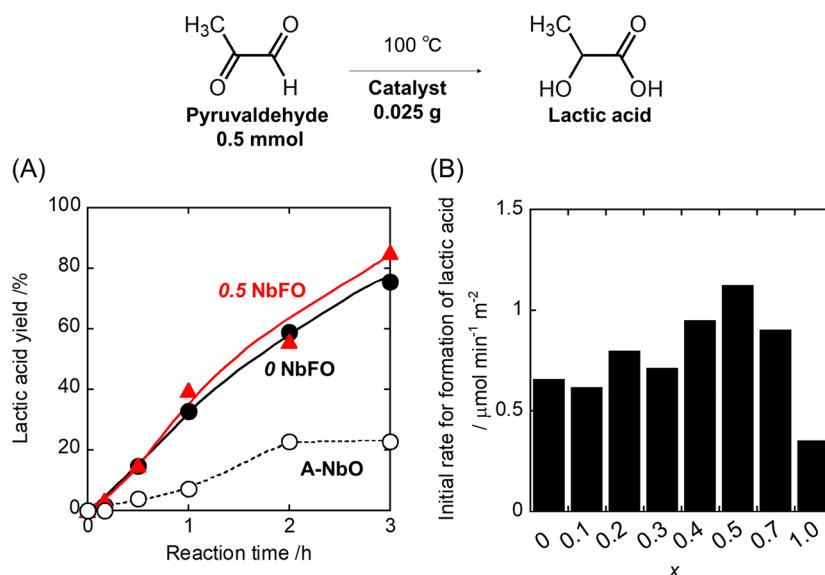


**Figure 7.** (A) Lactic acid yields as a function of reaction time over A-NbO, 0NbFO, and 0.5NbFO. (B) Initial formation rate of lactic acid over  $x\text{NbFO}$ .

basis of these facts, we here propose that the micropore sites can work as B sites to catalyze this reaction. The local catalyst structure around the heptagonal channel might be crucial for the catalysis, since a significant decrease in activity was observed at  $0.7 \leq x$ , in which hexagonal textures derived from the  $\text{HTB-Nb}(\text{F},\text{O})_x$  moieties was observed by XRD patterns (Figure 2D) and HAADF-STEM images (Figure 3). Arrhenius plots over 0NbFO and 0.5NbFO in the temperature range of 80–110 °C were obtained (Figure S10). While these catalysts showed comparable activation energies (0NbFO, 129.3 kJ/mol; 0.5NbFO, 127.9 kJ/mol), an almost 3-fold difference was observed in their frequency factors (0NbFO,  $0.99 \mu\text{mol min}^{-1} \text{m}^{-2}$ ; 0.5NbFO,  $2.44 \mu\text{mol min}^{-1} \text{m}^{-2}$ ), implying that the activity difference between 0NbFO and 0.5NbFO is derived from the increase in the number of catalytically active sites. The decrease in the catalytic activity at  $0.7 \leq x$  is most probably caused by the concomitant formation of the  $\text{HTB-Nb}(\text{F},\text{O})_x$  phase with HDS-NbO.

Nakajima et al. discovered that  $\text{Nb}_2\text{O}_5 \cdot n\text{H}_2\text{O}$  has water-tolerant Lewis acidity that can catalyze acid reactions relating to the Lewis acid site even in the presence of water.<sup>4</sup> We recently reported that 0NbFO showed water-tolerant Lewis acidity that can catalyze the transformation of pyruvaldehyde to lactic acid and the dehydration of xylose to form furfural even in the presence of water.<sup>10</sup> Here, we tested the transformation of pyruvaldehyde to lactic acid in order to evaluate the catalytic activity over the  $x\text{NbFO}$  catalyst for Lewis acid reaction in the presence of water. Figure 7A shows the changes in lactic acid yield with reaction time over 0NbFO, 0.5NbFO, and A-NbO. As we reported previously, 0NbFO and A-NbO promoted the formation of lactic acid. The catalytic activity of 0NbFO was clearly superior to that of A-NbO, and the lactic acid yields at 3 h from the start of the reaction were 22.7% over A-NbO and 75.5% over 0NbFO. 0.5NbFO showed catalytic activity comparable to that of 0NbFO, and the lactic acid yield at 3 h was 85.4%. Figure 7B shows the initial formation rate of lactic acid over  $x\text{NbFO}$  on the basis of surface area. The reaction rate was obtained in the range in which lactic acid yield increases linearly with reaction time (Figure S11). In 0NbFO, the initial reaction rate per surface

area was  $0.66 \mu\text{mol min}^{-1} \text{m}^{-2}$ . This rate continuously increased with an increase in  $x$ , and the rate became  $1.12 \mu\text{mol min}^{-1} \text{m}^{-2}$  over 0.5NbFO. On the other hand, the rate was significantly decreased by a further increase in  $x$  and the rate was  $0.35 \mu\text{mol min}^{-1} \text{m}^{-2}$  over 1.0NbFO. The catalytic activity changed with  $x$  in a manner similar to the B reaction, suggesting that the micropore sites over the HDS-NbO catalyst provided the water-tolerant Lewis acid sites related to the catalysis. We reported that the local structure around the heptagonal channel site can form oxygen defect sites.<sup>34–36</sup> According to that report, it can be speculated that the oxygen defect sites around micropore sites form coordinatively unsaturated sites workable as L sites even in the presence of water. Furthermore, the local catalyst structure around the heptagonal channel site should be crucial for this catalytic reaction, since the catalytic activity decreased at  $0.7 \leq x$  possibly due to the coformation of the  $\text{HTB-Nb}(\text{F},\text{O})_x$  moieties that is constituted by the arrangement of the hexagonal channels.

On the basis of the above facts, we suggest here that the B site and L site generated over the micropore sites, particularly over the heptagonal channel site, can work as the catalytically active sites. A crucial role of the local catalyst structure in acid reactions was clarified (Figure 8).

#### 4. CONCLUSION

High dimensionally structured Nb oxide (HDS-NbO) containing F<sup>-</sup> was synthesized by the addition of  $\text{NH}_4\text{F}$  in hydrothermal synthesis. F<sup>-</sup> was located by replacing the lattice oxygen in the HDS-NbO structure, and the amount of F<sup>-</sup> could be increased up to an F<sup>-</sup>/Nb ratio of 0.55. Interestingly, the local catalyst structure was changed by the introduction of F<sup>-</sup> so as to increase the number of micropores including hexagonal and heptagonal channels. The introduction of an appropriate amount of F<sup>-</sup> substantially increased the catalytic activity for Brønsted reactions, as evaluated by Friedel–Crafts alkylation. However, the catalytic activity was decreased by excess addition of F<sup>-</sup>. Almost the same trend was observed in the water-tolerant Lewis acid reaction, as evaluated by the transformation of pyruvaldehyde to lactic acid. On the basis of

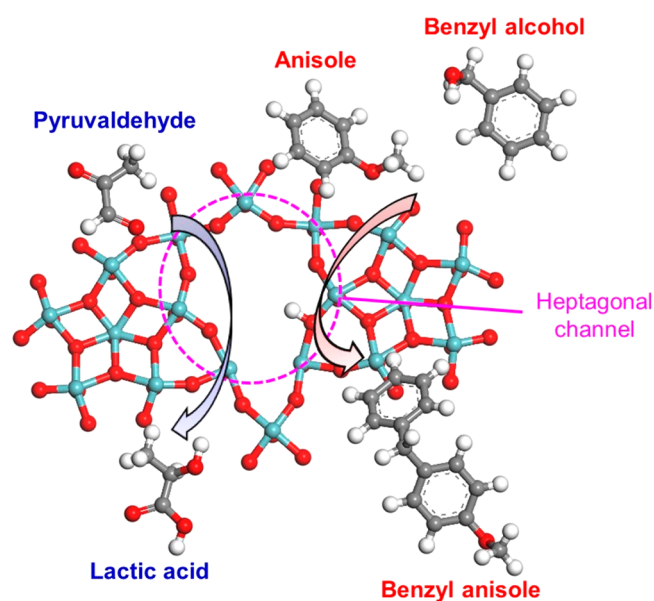


**Figure 8.** Image of the B reaction and L reaction over the heptagonal channel of HDS-NbO. Color scheme: Nb, light blue; O, red; C, gray; H, white.

the local catalyst structure and the catalytic activity, we suggest that the Brønsted acid sites and Lewis acid sites formed around the heptagonal channel work as the catalytically active sites for these reactions. We conclude that the local catalyst structure formed in the crystal structure is crucial for the catalysis of the above acid reactions.

## ■ ASSOCIATED CONTENT

### Supporting Information

The Supporting Information is available free of charge at <https://pubs.acs.org/doi/10.1021/acs.inorgchem.0c00949>.

Results of Hammett indicator over  $x$ NbFO, XRD patterns of 0NbFO, 0.5NbFO, and 0NbFO synthesized with  $(\text{NH}_4)_2\text{SO}_4$ , SEM images of 0NbFO, 0.5NbFO, and 1.0NbFO, lattice parameter changes as a function of F/Nb ratio in  $x$ NbFO after air calcination, TPD profiles of  $x$ NbFO for  $\text{NH}_3$  desorption, IR spectra of  $x$ NbFO before and after air calcination, weight loss of 0NbFO and 0.5NbFO after the pyridine adsorption IR experiment, ratio of IR band area of the Lewis acid sites and Brønsted acid sites over  $x$ NbFO, IR spectrum of A-NbO after the pyridine adsorption and its TG profile after the pyridine adsorption IR experiment, initial amount of benzyl anisole formed over  $x$ NbFO on the basis of surface area as a function of reaction time, Arrhenius plot for benzyl anisole formation over 0NbFO and 0.5NbFO, and initial amount of lactic acid formed over  $x$ NbFO on the basis of surface area as a function of reaction time (PDF)

## ■ AUTHOR INFORMATION

### Corresponding Authors

**Satoshi Ishikawa** – Department of Material and Life Chemistry, Faculty of Engineering, Kanagawa University, Yokohama 221-8686, Japan; [orcid.org/0000-0003-4372-4108](https://orcid.org/0000-0003-4372-4108); Email: [sishikawa@kanagawa-u.ac.jp](mailto:sishikawa@kanagawa-u.ac.jp)

**Wataru Ueda** – Department of Material and Life Chemistry, Faculty of Engineering, Kanagawa University, Yokohama 221-8686, Japan; Email: [uedaw@kanagawa-u.ac.jp](mailto:uedaw@kanagawa-u.ac.jp)

### Authors

**Mai Shinoda** – Department of Material and Life Chemistry, Faculty of Engineering, Kanagawa University, Yokohama 221-8686, Japan

**Yuta Motoki** – Department of Material and Life Chemistry, Faculty of Engineering, Kanagawa University, Yokohama 221-8686, Japan

**Shota Tsurumi** – Department of Material and Life Chemistry, Faculty of Engineering, Kanagawa University, Yokohama 221-8686, Japan

**Momoka Kimura** – Department of Material and Life Chemistry, Faculty of Engineering, Kanagawa University, Yokohama 221-8686, Japan

**Norihito Hiyoshi** – National Institute of Advanced Industrial Science and Technology (AIST), Sendai 983-8551, Japan; [orcid.org/0000-0001-7855-8643](https://orcid.org/0000-0001-7855-8643)

**Akihiro Yoshida** – Institute of Regional Innovation, Hirosaki University, Aomori 030-0813, Japan

Complete contact information is available at: <https://pubs.acs.org/doi/10.1021/acs.inorgchem.0c00949>

### Author Contributions

The manuscript was written through contributions by all authors. All authors have given approval to the final version of the manuscript.

### Notes

The authors declare no competing financial interest.

## ■ ACKNOWLEDGMENTS

This work was supported by JSPS KAKENHI Grant Number 15H0-2318.

## ■ REFERENCES

- (1) Tanabe, K.; Okazaki, S. Various Reactions Catalyzed by Niobium Compounds and Materials. *Appl. Catal., A* **1995**, *133*, 191–218.
- (2) Tanabe, K. Catalytic Application of Niobium Compounds. *Catal. Today* **2003**, *78*, 65–77.
- (3) Kitano, T.; Shishido, T.; Teramura, K.; Tanaka, T. Brønsted Acid Property of Alumina-Supported Niobium Oxide Calcined at High Temperatures: Characterization by Acid-Catalyzed Reactions and Spectroscopic Methods. *J. Phys. Chem. C* **2012**, *116*, 11615–11625.
- (4) Nakajima, K.; Baba, Y.; Noma, R.; Kitano, M.; Kondo, J. N.; Hayashi, S.; Hara, M.  $\text{Nb}_2\text{O}_5 \cdot n\text{H}_2\text{O}$  as a Heterogeneous Catalyst with Water-Tolerant Lewis Acid Sites. *J. Am. Chem. Soc.* **2011**, *133*, 4224–4227.
- (5) Fan, W.; Zhang, Q.; Deng, W.; Wang, Y. Niobic Acid Nanosheets Synthesized by a Simple Hydrothermal Method as Efficient Brønsted Acid Catalysts. *Chem. Mater.* **2013**, *25*, 3277–3287.
- (6) Kreissl, H. T.; Li, M. M. J.; Peng, Y. K.; Nakagawa, K.; Hooper, T. J. N.; Hanna, J. V.; Shepherd, A.; Wu, T. S.; Soo, Y. L.; Tsang, S. C. E. Structural Studies of Bulk to Nanosize Niobium Oxides with Correlation to Their Acidity. *J. Am. Chem. Soc.* **2017**, *139*, 12670–12680.
- (7) Hirunsit, P.; Toyao, T.; Siddiki, S. M. A. H.; Shimizu, K.; Ehara, M. Origin of  $\text{Nb}_2\text{O}_5$  Lewis Acid Catalysis for Activation of Carboxylic Acids in the Presence of a Hard Base. *ChemPhysChem* **2018**, *19*, 2848–2857.
- (8) Siddiki, S. M. A. H.; Rashed, M. N.; Ali, M. A.; Toyao, T.; hirunsit, P.; Ehara, M.; Shimizu, K. Lewis Acid Catalysis of  $\text{Nb}_2\text{O}_5$  for

Reactions of Carboxylic Acid Derivatives in the Presence of Basic Inhibitors. *ChemCatChem* **2019**, *11*, 383–396.

(9) Murayama, T.; Chen, J.; Hirata, J.; Matsumoto, K.; Ueda, W. Hydrothermal Synthesis of Octahedra-based Layered Niobium Oxide and its Catalytic Activity as a Solid Acid. *Catal. Sci. Technol.* **2014**, *4*, 4250–4257.

(10) Nakajima, K.; Hirata, J.; Kim, M.; Gupta, N. K.; Murayama, T.; Yoshida, A.; Hiyoshi, N.; Fukuoka, A.; Ueda, W. Facile Formation of Lactic Acid from a Triose Sugar in Water over Niobium Oxide with a Deformed Orthorhombic Phase. *ACS Catal.* **2018**, *8*, 283–290.

(11) Emeis, C. A. Determination of Integrated Molar Extinction Coefficients for Infrared Absorption Bands of Pyridine Adsorbed on Solid Acid Catalysts. *J. Catal.* **1993**, *141*, 347–354.

(12) Kondo, J. N.; Nishitani, R.; Yoda, E.; Yokoi, T.; Tatsumi, T.; Domen, K. A Comparative IR Characterization of Acidic Sites on HY Zeolite by Pyridine and CO Probes with Silica-Alumina and  $\gamma$ -Alumina References. *Phys. Chem. Chem. Phys.* **2010**, *12*, 11576–11586.

(13) Newman, A. D.; Brown, D. R.; Siril, P.; Lee, A. F.; Wilson, K. Structural Studies of High Dispersion  $\text{H}_3\text{PW}_{12}\text{O}_{40}/\text{SiO}_2$  Solid Acid Catalysts. *Phys. Chem. Chem. Phys.* **2006**, *8*, 2893–2902.

(14) Konya, T.; Katou, T.; Murayama, T.; Ishikawa, S.; Sadakane, M.; Buttrey, D.; Ueda, W. An Orthorhombic  $\text{Mo}_3\text{VO}_x$  catalyst most active for oxidative dehydrogenation of ethane among related complex metal oxides. *Catal. Sci. Technol.* **2013**, *3* (2), 380–387.

(15) Shimoda, K.; Ishikawa, S.; Tashiro, M.; Kumaki, M.; Hiyoshi, N.; Ueda, W. Synthesis of High Dimensionally Structured Mo-Fe Mixed Metal Oxide and Its Catalytic Activity for Selective Oxidation of Methanol. *Inorg. Chem.* **2020**, *59* (8), 5252–5255.

(16) Szilágyi, I. M.; Madarász, J.; Pokol, G.; Király, P.; Tárkányi, G.; Saukko, S.; Mizsei, J.; Tóth, A. L.; Szabá, A.; Josepovits, K. V. Stability and Controlled Composition of Hexagonal  $\text{WO}_3$ . *Chem. Mater.* **2008**, *20*, 4116–4125.

(17) Phuruangrat, A.; Ham, D. J.; Hong, S. J.; Thongtem, S.; Lee, J. S. Synthesis of Hexagonal  $\text{WO}_3$  Nanowires by Microwave-Assisted Hydrothermal Method and their Electrocatalytic Activities for Hydrogen Evolution Reaction. *J. Mater. Chem.* **2010**, *20*, 1683–1690.

(18) Sadakane, M.; Kodato, K.; Kuranishi, T.; Nodasaka, Y.; Sugawara, K.; Sakaguchi, N.; Nagai, T.; Matsui, Y.; Ueda, W. Molybdenum-Vanadium-based Molecular Sieves with Microchannels of Seven-Membered Rings of Corner-Sharing Metal Oxide Octahedra. *Angew. Chem., Int. Ed.* **2008**, *47*, 2493–2496.

(19) Sadakane, M.; Ohmura, S.; Kodato, K.; Fujisawa, T.; Kato, K.; Shimidzu, K.; Murayama, T.; Ueda, W. Redox Tunable Reversible Molecular Sieves: Orthorhombic Molybdenum Vanadium Oxide. *Chem. Commun.* **2011**, *47*, 10812–10814.

(20) Ishikawa, S.; Yi, X.; Murayama, T.; Ueda, W. Heptagonal Channel Micropore of Orthorhombic  $\text{Mo}_3\text{VO}_x$  as Catalysis Field for the Selective Oxidation of Ethane. *Appl. Catal., A* **2014**, *474*, 10–17.

(21) Cheetham, A. K.; Férey, G.; Loiseau, T. Open-Framework Inorganic Materials. *Angew. Chem., Int. Ed.* **1999**, *38*, 3268–3292.

(22) Paulet, C.; Loiseau, T.; Férey, G. Hydrothermal Synthesis (in Water-Dimethylformamide) and Crystal Structure of MIL-30, A New Layered Fluorinated Gallium Phosphate with 1,3-Diaminopropane and Dimethylamine as Templates. *J. Mater. Chem.* **2000**, *10*, 1225–1229.

(23) Agulyansky, A. *Chemistry of Tantalum and Niobium Fluoride Compounds*; Elsevier: Oxford, 2004; pp 125–134.

(24) Rodriguez-Gonzalez, L.; Hermes, F.; Bertmer, M.; Rodriguez-Castellon, E.; Jimenez-Lopez, A.; Simon, U. The Acid Properties of H-ZSM-5 as Studied by  $\text{NH}_3$ -TPD and  $^{27}\text{Al}$ -MAS-NMR Spectroscopy. *Appl. Catal., A* **2007**, *328*, 174–182.

(25) Liu, D.; Yuan, P.; Liu, H.; Cai, J.; Tan, D.; He, H.; Zhu, J.; Chen, T. Quantitative Characterization of the Solid Acidity of Montmorillonite using Combined FTIR and TPD based on the  $\text{NH}_3$  Adsorption System. *Appl. Clay Sci.* **2013**, *80–81*, 407–412.

(26) Katada, N.; Tamagawa, H.; Niwa, M. Quantitative Analysis of Acidic OH groups in Zeolite by Ammonia IRMS-TPD and DFT: Application to BEA. *Catal. Today* **2014**, *226*, 37–46.

(27) Kitano, T.; Shishido, T.; Teramura, K.; Tanaka, T. Characterization of Thermally Stable Bronsted Acid Sites on Alumina-Supported Niobium Oxide after Calcination at High Temperatures. *ChemPhysChem* **2013**, *14*, 2560–2569.

(28) Tamura, M.; Shimizu, K.; Satsuma, A. Comprehensive IR Study on Acid/Base Properties of Metal Oxides. *Appl. Catal., A* **2012**, *433–434*, 135–145.

(29) Yamamoto, T.; Tanaka, T.; Matsuyama, T.; Funabiki, T.; Yoshida, S. Alumina-Supported Rare-Earth Oxides Characterized by Acid-Catalyzed Reactions and Spectroscopic Methods. *J. Phys. Chem. B* **2001**, *105*, 1908–1916.

(30) Morterra, C.; Magnacca, G. A Case Study: Surface Chemistry and Surface Structure of Catalytic Aluminas, as Studied by Vibrational Spectroscopy of Adsorbed Species. *Catal. Today* **1996**, *27*, 497–532.

(31) Tagusagawa, C.; Takagaki, A.; Iguchi, A.; Takanabe, K.; Kondo, J. N.; Ebitani, K.; Hayashi, S.; Tatsumi, T.; Domen, K. Highly Active Mesoporous Nb–W Oxide Solid-Acid Catalyst. *Angew. Chem., Int. Ed.* **2010**, *49*, 1128–1132.

(32) Okumura, K.; Yamashita, K.; Hirano, M.; Niwa, M. Active and Reusable Catalyst in the Friedel-Crafts Alkylation Derived from a Heteropoly Acid. *Chem. Lett.* **2005**, *34*, 716–717.

(33) Buffon, R.; Auroux, A.; Lefebvre, F.; Leconte, M.; Choplin, A.; Basset, J. M. A Surface Organometallic Approach to the Synthesis of Rhenium-based Catalysts for the Metathesis of Olefins:  $\text{CH}_3\text{ReO}_3/\text{Nb}_2\text{O}_5$ . *J. Mol. Catal.* **1992**, *76*, 287–295.

(34) Ishikawa, S.; Kobayashi, D.; Konya, T.; Ohmura, S.; Murayama, T.; Yasuda, N.; Sadakane, M.; Ueda, W. Redox Treatment of Orthorhombic  $\text{Mo}_{29}\text{V}_{11}\text{O}_{112}$  and Relationships between Crystal Structure, Microporosity and Catalytic Performance for Selective Oxidation of Ethane. *J. Phys. Chem. C* **2015**, *119*, 7195–7206.

(35) Ishikawa, S.; Ueda, W. Microporous Crystalline Mo-V Mixed Oxides for Selective Oxidations. *Catal. Sci. Technol.* **2016**, *6*, 617–629.

(36) Ishikawa, S.; Zhang, Z.; Ueda, W. Unit Synthesis Approach for Creating High Dimensionally Structured Complex Metal Oxides as Catalysts for Selective Oxidations. *ACS Catal.* **2018**, *8*, 2935–2943.